Laser particle sizer for plume-induced ejecta clouds

R. E. Peale,[a,b] C. J. Fredricksen,[b] C. L. Barrett,[b] A. G. Otero,[b] A. R. Jack,[a] F. J. Gonzalez,[b] D. Sapkota,[c] A. R. Dove,[a] P. T. Metzger.[c]

[a]Physics, University of Central Florida, Orlando FL 32816, USA, Robert.peale@ucf.edu;
[b]Truventic, Orlando FL 32805, USA; [c]Florida Space Institute, University of Central Florida, Orlando FL 32826, USA

ABSTRACT

Surface dust blown by a lunar lander can spoof sensors and damage lander and other surface and orbital assets. Since many countries seek to use and leverage the Moon in the coming decades, this is potentially a defense issue. Empirical data on Plume Surface Interactions (PSI) from lander-mounted instruments are needed to determine particle size distributions. We report a feasibility study of laser light-scattering for particle sizing. Calculations suggest that distributions of particle sizes in the range 0.1 to 10 microns can be accurately determined from laser-propagation decay using 4 to 8 wavelengths between 0.4 to 2 microns. Lab standards have been created based on calibrated showers of silica spheres and known concentrations and sizes of SiC grit in resin rods. Experiments were performed using lasers from 0.4 to 10 micron wavelength. For visible wavelengths, a point Si detector or images taken with a Si CCD camera were used to record scattered intensity vs propagation distance. At long-wave infrared, a pyroelectric detector or bolometer array were used. Characteristic decay lengths were determined by an algebraic sliding aperture method suitable for rapid and automated analysis. The experiments confirm theoretical expectations for Mie scattering by simple distributions of spherical particles. These results inform future experiments for testing the inverse problem of extracting more complicated size distributions from decay lengths measured using multiple wavelengths.

1. INTRODUCTION

Lunar lander plume ejecta transport is poorly understood. Problems include soil erosion under conditions of supersonic flow, transitionally rarefied gas lacking viscosity and lacking a conventional boundary layer or turbulence spectrum, low gravity, and irregular particles unsmoothed by conventional weathering [1]. Empirical data is needed to inform models and solve the erosion physics.

Flow codes predict plume-surface interaction (PSI) phenomena [2-4], but unsolved parts are represented by empirical correlations [5-10], and the data remain severely limited. Terrestrial granular physics experiments must discard parts of the physics when scaling to the smallest needed grain size. Injecting large-scale supersonic gas plumes into a chamber under lunar vacuum and simulated low gravity is impractical. Therefore, high-quality data must be collected from actual Moon landings.

Lunar dust clouds have a broad distribution of particle sizes, spanning many orders of magnitude and traveling with relative velocities correlated to their sizes [11-13]. Size-dependent scattering [14] and size segregation [15] determine local size distributions of entrained particulates and the local momentum transfer between the particles and plume gases. Ultimately, this particle-scale behavior governs the ejecta transport and is included in NASA's Gas Granular Flow Solver [3,4], but particle-scale lander-plume measurements are still needed.

Damage to surface assets by plume-blown dust was revealed in returned coupons from Lunar Surveyor III, which was scoured and pitted by dust during Apollo 12's Lunar Module (LM) landing [15]. Some fraction of the dust may reach escape velocities [16] and altitudes at which they can even damage orbital assets. Dust clouds obscure the view of optical sensors [17].

Many countries seek to use and leverage the Moon. Damage caused by blown dust may ignite international conflicts, or it may prevent the establishment of permanent bases. The scientific value of the eroded surface is compromised. The temporally and spatially variable particle size distribution in lunar plumes has never been measured accurately. Estimates depend heavily on assumptions and modeling. Accurate data is to predict and prevent damage, answer

questions about transport, constrain models, reveal soil erosion rates, and understand size segregation. A lander-mounted laser-based particle sizer can help provide such data.

We report calculations that determine particle size distributions from a laser propagation decay at a number of wavelengths. A significant result is that relevant distributions can be accurately determined using as few as 4 visible and near IR wavelengths. Laboratory experiments on scattering standards validate the theory and inform the design of a lander-mounted system to acquire beam propagation lengths under various known monodisperse size, concentration, mineralogy, and wavelength regimes. An algebraic means of extracting beam propagation decay lengths from images of scattered light was demonstrated with potential application to real-time analysis.

2. THEORY

For homogeneous distributions in the single-particle scattering limit, the beam intensity decays exponentially with distance z as $Exp(-\mu(\lambda) z)$ [18], where the decay constant is

$$\mu(\lambda) = \int n(a)\pi a^2 Q_{ext}(a,\lambda)da \quad . \tag{1}$$

$n(a)\,da$ is the number of particles with radius between a and $a + da$ per unit volume. The units of μ are inverse length, and μ^{-1} is the characteristic beam propagation decay length. The extinction efficiency factor Q_{ext} is the ratio of extinction cross section to physical cross section πa^2 for spheres. For given optical constants of the mineral, and assuming spheres, it is a universal function of the dimensionless parameter $x = 2\pi a/\lambda$.

Figure 1 (left) presents a plot of Q_{ext} vs x for two values of real index m. The curve rises as x^4 in the small-x Rayleigh regime [18, sec 6.31], followed by a series of diminishing oscillations that converge on the value 2. For larger index, the oscillation period shortens, and the curve contracts toward smaller x. For the common lunar mineral Olivine with m = 1.7, the peak occurs near $x = 3$. For the complicated mineralogy of the space-weathered lunar regolith featuring randomly shaped and oriented particles, we expect the ringing in Q_{ext} to be smeared out. We may reasonably suppose that $Q_{ext}(x)$ should rise sharply up to a value of about 3 near $x = 3$, and then drop smoothly to the value of 2 by $x \sim 40$.
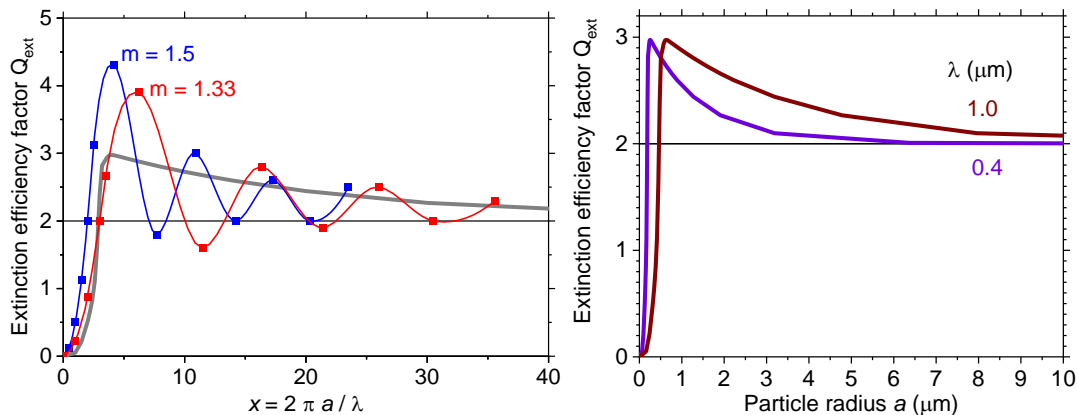

Figure 1. (left) single-particle $Q_{ext}(x)$ for the indicated real indices and hypothetical curve for a mixture. (right) Extinction efficiency factor as function of particle radius for two wavelengths.

A mathematical representation of a hypothetical smoothed $Q_{ext}(x)$ function is useful for calculations. Lacking information on the actual curve, an ad hoc function that approximates the likely shape will suffice. Figure 1 (right) presents a plot of such a function comprising the sum of two terms. First, a $\sin^4(x)$ function captures the expected x^4 dependence in the small-x Rayleigh regime, followed by a transition to a rounded peak. The coefficient in Rayleigh scattering is of order unity and independent of wavelength if there is no dispersion. A Heaviside factor truncates the oscillations beyond half a period. The second term is an offset decaying exponential with a second Heaviside factor to truncate below $x \sim 3$. The Heaviside functions are represented by $1/(1+\exp(-b(x-x_0)))$, and unity minus this function, where the constants b and x_0 are manually adjusted for each to obtain a reasonable shape. Figure 1 (right) presents the Q_{ext} curves as a function of particle *radius* for two wavelengths. Each curve peaks at $\sim \lambda/2$. Beyond the peak, the transition to the value 2 is slower for the longer wavelength.

Figure 2 (left) presents a log-log plot of the extinction cross section $\pi a^2 Q_{ext}$. For radii $a < \sim \lambda/2$, the curves rise with a as $\sim 300 \lambda^{-4} a^6$. For $a > \sim \lambda/2$, the curves rise more slowly as $2\pi a^2$, independent of λ. To estimate the extinction constant $\mu(\lambda)$, it is necessary to integrate the product of the cross section curves and particle density. While scattering theory is presented in terms of particle radius a, number density data is usually presented in terms of particle diameter $D = 2a$. Figure 2 (right) presents probability density for a lunar soil sample determined from data published in [19]. In that paper, data for the unitless probability function $P_{log} = (1/n_T) dn/d[\log(D)]$ was plotted, where n_T is the total particle concentration. The probability density is given by $P_{lin}(D) = P_{log}/D$, which has units of inverse length. The number density of particles with diameters between D and D+dD is then $n_T P_{lin}(D)$ dD.
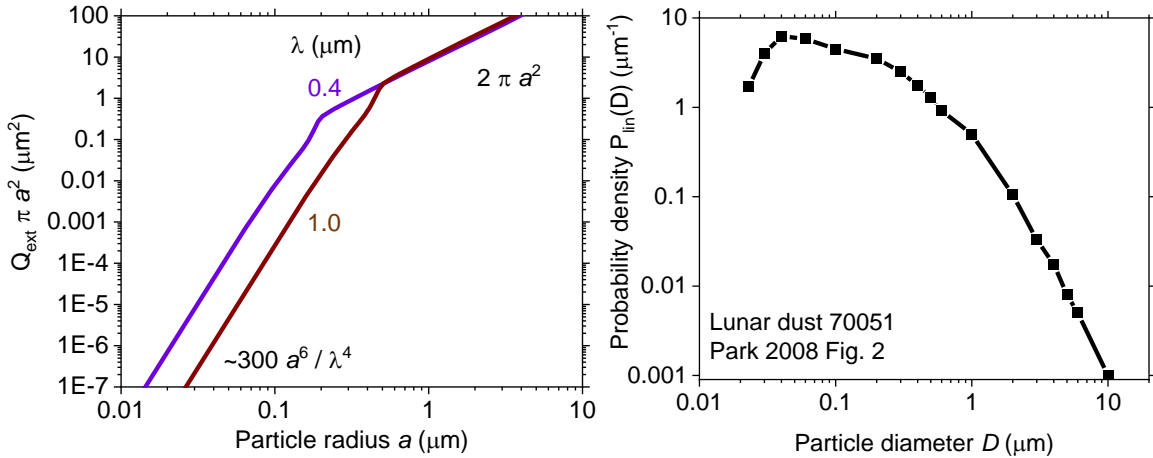

Figure 2. (left) Extinction cross section vs particle radius for two wavelengths. (right) Representative size probability density of a lunar soil sample [19].

Figure 3 presents a plot for the product of probability density and extinction cross section based on the curves in Figure 2 (left) and the lunar size distribution points in Figure 2 (right) for wavelengths 0.4 and 1 μm. The curves represent the integrand of Eq. (1).

A first observation from Figure 3 is that for diameter greater than about 0.6 times the longer wavelength, the two curves are identical. That is because $Q_{ext} = 2\pi a^2$ is the same for both curves from about this point onward, according to Figure 2 (left).
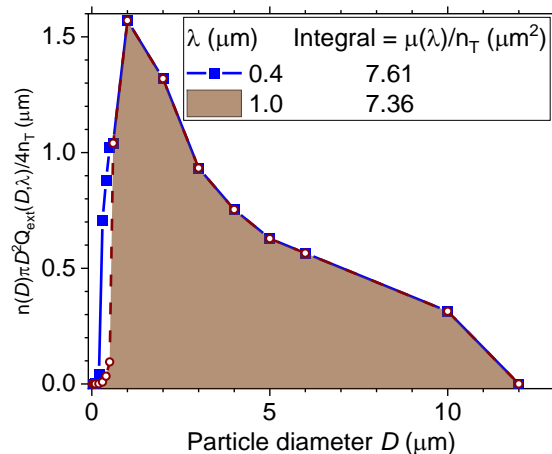

Figure 3. Integrand of Eq. (1) at two wavelengths for a lunar soil size distribution

A second observation is that particles with diameters less than about 0.2 λ contribute almost nothing to the integral and decay constant. This means that the lower integration limit in Eq. (1) may be set to this value. The error associated with this choice is much less than any likely experimental uncertainties.

A third observation is that the values of $\mu(\lambda)/n_T$ are the areas $A(\lambda)$ under the respective curves for the given size probability distribution. Values for this integral given in the legend were obtained using Origin plotting software and were checked by graphical estimation. Thus, for the assumed particle distribution, a measurement of $\mu(\lambda)$ gives the concentration of particles with diameters greater than $\lambda/2$. In other words, $n(D > \lambda/2) = \mu(\lambda)/A(\lambda)$. Alternatively, if a homogeneous dust cloud with the same size probability distribution contains 10000 per cc of particles diameter exceeding $\lambda/2$, then the propagation decay length is 13 meters at 0.4 μm wavelength. This informs the feasibility for imaging laser propagation from a lander mounted camera.

By measuring $\mu(\lambda)$ using lasers of various wavelengths, one may map out the relative probability distribution in an approach that is similar to finding size distributions by sieving. If we enumerate and order the wavelengths by the index i, then by Eq. (1) we have

$$\mu(\lambda_{i+1}) - \mu(\lambda_i) = \left(\frac{\pi n_T}{4}\right) P(D_i) \int_{0.2\lambda_i}^{0.6\lambda_{i+1}} [Q_{ext}(D, \lambda_{i+1}) - Q_{ext}(D, \lambda_i)] D^2 dD \qquad (2)$$

The lower limit on the integral for $\mu(\lambda_{i+1})$ was reduced from 0.2 λ_{i+1} to 0.2 λ_i, which has essentially no effect on the result. The integrand is a universal function of D/λ and gives a number A_i that should be weakly dependent on the exact values of the limits. Note that the bracketed quantity in the integral is negative as is the left side of Eq. (2). After making some obvious simplifications in notation, the probability density is

$$P(D_i) = \left(\frac{4}{\pi n_T}\right) \frac{\mu_{i+1} - \mu_i}{A_i} \qquad . \qquad (3)$$

Both numerator and denominator of Eq. (3) are negative, so $P(D_i)$ is positive. Until n_T is known, Eq. (3) gives relative probabilities. Such information would already tell something about size segregation and whether the dust distribution differs significantly from that of typical soil. Knowing the relative probabilities, the total concentration n_T for particles of all sizes might be independently determined from the brightness of scattered light of one wavelength at a given point in the plume.

An alternate approach is based on matrix inversion. We consider i_{max} discrete laser wavelengths and the same number of discrete particle size bins a_j with widths Δa_j. This gives i_{max} unknowns $n_j = n(a_j)\Delta a_j$, which are the number of particles per unit volume in each bin. We have the same number of equations for the measured $\mu_i = \mu(\lambda_i)$, namely

$$\mu_i = \sum_j \pi a_j^2 Q_{ext}(a_j, \lambda_i) n_j = A_{ij} n_j . \qquad (4)$$

In the last equality, summation over the j size bins is implied, and the extinction cross section matrix $A_{ij} = \pi a_j^2 Q_{ext}(a_j, \lambda_i)$. The solution to our problem is $n_j = A_{ij}^{-1} \mu_i$. The expected rapid decrease in n_j as a_j increases complicates the inversion to find n_j. A solution [20] factors the probability distribution into a power law h(D) times a slow modulation f(D), which can be solved for. Figure 4 (left) shows that with as few as four wavelengths between 0.4 and 1.8 μm, this method reproduces a model probability distribution for lunar soil [21]. Figure 4 (right), a semi-log plot of contribution to opacity $(\pi D^2/4) P(D)$ for dD = 1 μm, shows results for a more sharply peaked distribution that is depleted of large particles. For this more rapidly varying situation more wavelengths are needed.
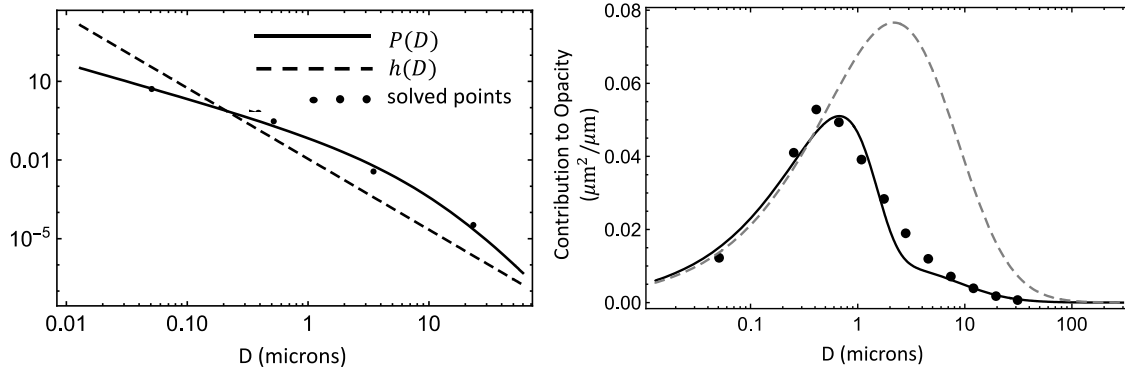

Figure 4. Particle diameter probability distribution for lunar soil $P_L(D)$ with fast power law $h_L(D)$ and symbols for the best-fit solution with four laser wavelengths. (right) Solution for distribution depleted of large particles.

3. EXPERIMENT

We investigated two designs for laboratory standards. In the first, we dispersed SiC polishing grit in polyester resin, which was poured into molds and cured in the shape of rods. In the second, we dropped a shower of SiO_2 beads from a linear sieve. Photographs of these are presented in Figure 7. Scattered intensity was measured by translating a point detector or from images.
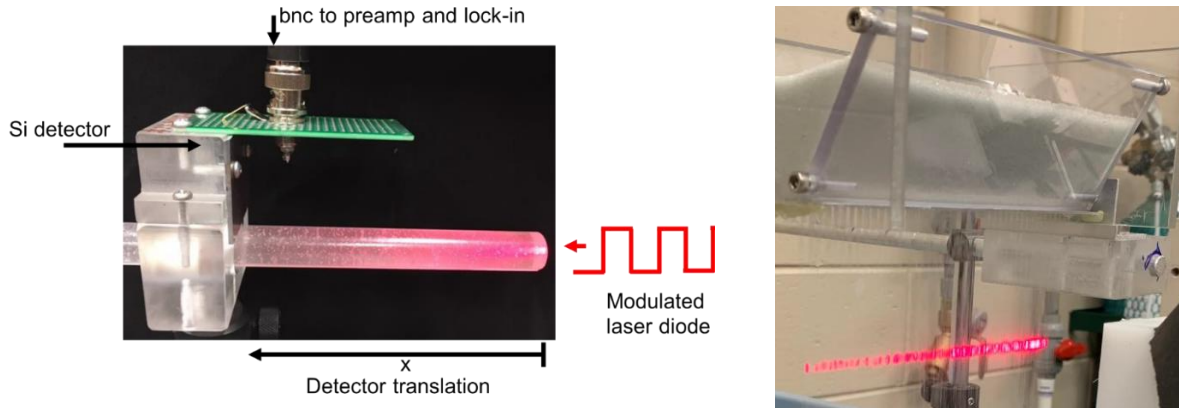

Figure 5. (left) Sliding point detector apparatus. (right) Bead fall set up.

Particle number density $n(D)dD$ is one of the key parameters in determining the decay constants, according to Eq. (1). For identical particles with individual mass m_p mixed into a volume V of resin the number density is $N = M/m_pV$, where M is the total mass of grit added to the liquid resin. The number density of particles that fall from a linear sieve is

$$N = \frac{\dot{M}}{m_p} \frac{1}{LW} \frac{1}{\sqrt{2gz}}$$

(5)

The numerator is the rate of mass of particles that are falling, which is measured with a scale and a timer. For a linear sieve, L is its length, W its width, g the acceleration of gravity, and z the distance of the beam below the openings that dispense the particles.

Our scattering experiments occurred in radius/wavelength regimes where the parameter x is at least 44 for SiC in resin, and up to 1300 for the glass bead fall. SiC's high 2.64 index scaled by the resin index 1.54 gives a relative index 1.7. Then according to Figure 1 (left), we may take extinction efficiency factor in all cases to have the value 2.

We used an algebraic method to determine the decay constant from the measured scattered intensity $I(x)$ as a function of distance x. The method involves no fitting routine, so that it may be fast and automated, and it is called the sliding aperture (SLAP) transform [22]. An experimental challenge is that the measured scattered laser intensity always sits on a background signal, e.g. scattered sunlight or electrical offset. This background is difficult to define, especially from the measured transient itself, and it adds an additional fitting factor and source of uncertainty that affects the determined value of μ. SLAP extracts decay rates independent of any unknown background. Scattered intensity I is measured at evenly spaced intervals along the beam path $x_m = m \, \Delta x$, giving intensity and rate vectors $I_m = I(x_m)$ and $r_m \equiv 1/x_m$. The SLAP transformed data with "aperture" = 2 is $X_m = X(r_m) \equiv I(2/r_m) - I(1/r_m) = I_{2m} - I_m$. A pure exponential decay with initial starting intensity $I(0)$ and baseline I_0, i.e. $I(x) = I(0) \exp(-\mu x) + I_0$, is SLAP transformed into a vector of values for the SLAP function of the rate vector as $X_m = I(0) (\exp(-2 \, \mu/r_m) - \exp(-\mu/r_m))$, which has a maximum value $X_{max} = I(0)[\exp(-2 \, \sigma_x) - \exp(-\sigma_x)] = I(0) \sigma_y$ at the rate $r_{max} = \mu/\ln(2) = \mu/\sigma_x$. The peak location in a plot of X/σ_y vs $\sigma_x r$ gives the decay rate μ. The value of the SLAP function at the peak gives the initial value of the decay $I(0)$ above the unknown baseline.

Figure 6 (left) presents an example scattering decay curve measured for a resin rod by the translated detector method with the parameters given in the figure text. We typically observe no polarization dependence for the decay constant. The decay length was calculated from Eq. (1) for a monodisperse distribution, assuming $Q_{ext} = 2$. The SLAP analysis of the decay constant is presented in Figure 6 (right). The SLAP value of the decay length is much closer to theoretical expectations than is the 1/e decay length, which is grossly underestimated because the baseline is poorly defined.
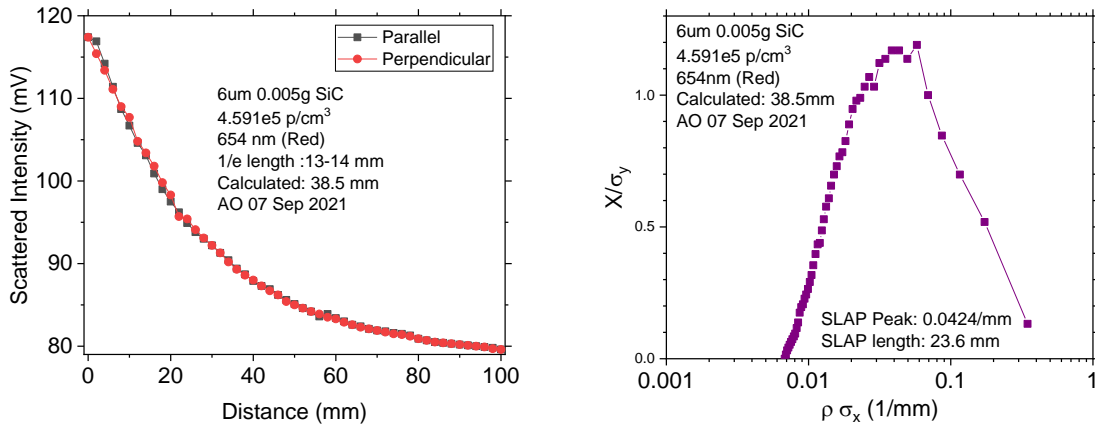

Figure 6. (left) Laser propagation decay curve for resin rod and (right) SLAP analysis.

Figure 7 compares calculated decay lengths (solid squares) to experimental values (open circles) for 654 nm laser wavelength. Results for other wavelengths are similar. The experimental values tend to fall below the predictions for the larger decay lengths. We believe that this artifact is due to the intrinsic extinction of the resin, including scattering by the inevitable bubbles. Since our minimum step size is mm for the sliding detector method, the rod standards appear limited to decay lengths between the values of 3 and 30 mm. Except for the 8 micron particles, the data in Figure 7 appear to track the size and concentration dependence rather well.
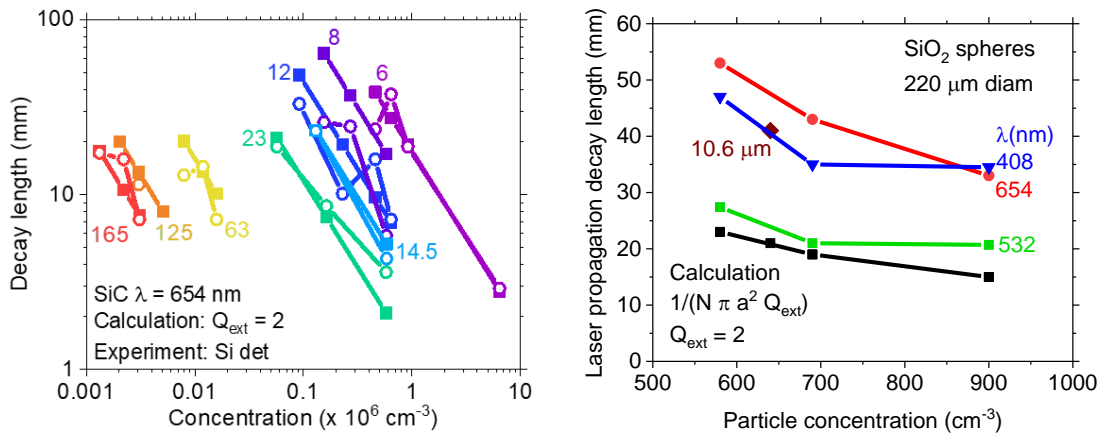

Figure 7. (left) Red laser propagation decay lengths vs particle concentration. Solid symbols are calculated, open symbols are measured for resin rod standards. Numbers next to the curves are particle diameters in microns. (right) Propagation decay length vs concentration for bead fall.

Figure 7 (right) compares measured decay lengths for four laser wavelengths with predictions of theory. Most of the measured values exceed the prediction by up to a factor of 2, which may be attributed in part to error in the estimation of bead concentration from Eq. (5). The predicted 1/N concentration dependence is consistent with the observations within the uncertainty.

SPIE USE: _____ DB Check, _____ Prod Check, Notes:

Alternative to a sliding point detector, we can extract decay lengths from images. The resulting plots are similar to Figure 7 (left), but there is more scatter in the experimental points. The additional uncertainty is due to a number of artifacts, such as saturation, internal reflection, reflection of background light off the rod surface, and angle dependence of the scattering.

4. DISCUSSION AND SUMMARY

Practically, a lander-mounted instrument would be limited to semiconductor diode lasers, which limits the wavelength range to approximately 0.4 - 2 μm. The Eq. (3) differencing approach would then be limited to sizes ranging from about 0.08 to 1.2 μm. Wavelengths at the long-wave end of this range would require a specialized imager, so the wavelength range might be even more restricted.

Even if lasers with wavelength beyond 2 μm were practical for a lander, the propagation decay lengths might become inconveniently long for imaging based on scattered light. This is due to the rapid depletion of larger particles in the soil distribution compounded by segregation processes. Besides being hard to image, long decay lengths are likely to exceed any plume homogeneity length scale.

The method of matrix inversion via the procedure in [20] promises to provide information about the particle size distribution over a wider range of sizes for the same set of wavelengths. This assertion is currently being investigated with more simulations and experiments.

In summary, preliminary theory and experiments were reported that support the use of a lander-mounted laser scatter device for determining particle size distribution in lander plumes. The calculations support the feasibility of using laser propagation decay lengths at small number of visible and near IR wavelengths to determine characteristic lunar particle distributions. Reported experimental results are first steps toward validating the proposed system in hardware.

ACKNOWLEDGEMENT AND DISCLOSURE

REFERENCES

1. Metzger, P. T., "Dust transport and its effects due to landing spacecraft," In: *Workshop on the Effects of Dust to Human Lunar Exploration*, Houston, TX, Feb. 11-13, 2020.
2. Tosh, A. , Liever, P. A., Arslanbekov, R. R., and Habchi S. D., "Numerical analysis of spacecraft rocket plume impingement under lunar environment," *J. Spacecraft and Rockets* 48, 93 (2011).
3. Gale, M., Buettner, K., Mehta, R., Liever, P. A., and Curtis, J., "Gas-Granular Flow Solver for Plume Surface Interaction and Cratering Simulations." *23rd AIAA Computational Fluid Dynamics Conf,*, p. 4503 (2017).
4. Liever, P. A., Gale, M. P., Mehta, R. S., and West, J. S., "Gas-Granular Simulation Framework for Spacecraft Landing Plume-Surface Interaction and Debris Transport Analysis," *Earth and Space* (2018): 39 (2018).
5. Metzger, P. T., Immer, C. D., Donahue, C. M., Vu, B. T., Latta III, R. C., Deyo-Svendsen, M., "Jet-induced cratering of a granular surface with application to lunar spaceports," *J. Aerospace Engineering* 22, 24 (2009).
6. Metzger, P. T., et al., "Craters Formed in Granular Beds by Impinging Jets of Gas," *Powders and Grains 2009*, Golden, Colorado.
7. Immer, C., and Metzger, P., "Rocket Cratering in Simulated Lunar and Martian Environments," *Earth and Space 2010*, Honolulu, HI.
8. LaMarche, C. Q., Metzger, P. T., and Curtis, J. S., "Cratering of a Lunar Soil Simulant, JSC-1A, by a Turbulent Subsonic Jet," *Earth and Space 2010*, Honolulu, HI.
9. Metzger, P. T., Smith, J., and Lane, J. E., "Phenomenology of soil erosion due to rocket exhaust on the Moon and the Mauna Kea lunar test site," *J. Geophysical Research – Planets* 116, E06005 (June 2011).
10. Metzger, P. T., "Rocket Exhaust Blowing Soil in Near Vacuum Conditions is Faster than Predicted by Continuum Scaling Laws," *Earth and Space* 2016, Orlando, FL.

11. Lane, J. E., Metzger, P. T., and Immer, C. D., "Lagrangian trajectory modeling of lunar dust particles," in Proc. 11th Biennial ASCE Aerospace Div. Intl. Conf. Engineering, Construction and Operations in Challenging Environments (Long Beach, California), Mar. 3-5, 2008.

12. Lane, J. E., Metzger, P. T. and Carlson, J. W., "Lunar Dust Particles Blown By Lander Engine Exhaust in Rarefied and Compressible Flow," *Earth and Space 2010*, Honolulu, HI.

13. Lane, J. E. and Metzger, P. T., "Ballistics Model for Particles on a Horizontal Plane in a Vacuum Propelled by a Vertically Impinging Gas Jet," *Particulate Sci. & Tech.* **30**, 196 (2012).

14. Anand, A., Berger, K. J., Metzger, P. T., and Hrenya, C. M., "Role of Collisions in Erosion of Regolith during a Lunar Landing," *Phys. Rev. E* 87, 022205 (2013).

15. Immer, C. D., Metzger, P., Hintze, P., Nick, A., and Horan, R., "Apollo 12 Lunar Module Exhaust Plume Impingement on Lunar Surveyor III," *Icarus* 211, 1089 (2011).

16. Metzger, P. T., Lane, J. E., Immer, C. D., Clements, C., "Cratering and blowing soil by rocket engines during lunar landings," H. Benaroya (Ed.), Lunar Settlements (CRC, Boca Raton, FL, 2010) p. 551.

17. Immer, C. D., Lane, J. E., Metzger, P. T., Clements, S., "Apollo video photogrammetry estimation of plume impingement effects," Proc. Earth and Space 2008, 11th Biennial ASCE Aerospace Div. Intl. Conf. Engineering, Construction and Operations in Challenging Environments, Long Beach, CA, Paper No. 1 (2008).

18. H. C. van de Hulst, Light Scattering by Small Particles, (Dover, New York, 1981).

19. Park, J., Liu, Y., Kihm, K., Taylor, L. A., "Characterization of Lunar Dust for Toxicological Studies. I: Particle Size Distribution," J. Aerospace Eng. 21, 266 (2008).

20. King, M. D., Byrne, D. M., Herman, B. M., Reagan, J. A., "Aerosol size distributions obtained by inversion of spectral optical depth measurements," J. Atmos. Sci. 35, 2153 (1978).

21. Metzger, P. T., Sapkota, D., Fox, J., and Bennett, N., "Aqua Factorem: Ultra Low Energy Lunar Water Extraction," final report, NASA Innovative Advanced Concepts (NIAC) Phase I, NASA grant no. 80NSSC20K1022, University of Central Florida, March 15, 2021.

22. Buchwald, W. R., Peale, R. E., Grant, P. C., Logan, J. V., Webster, P. T., Morath, C. P., "The sliding aperture transform and its applicability to deep level transient spectroscopy," manuscript (2022).